U.S. DEPARTMENT OF COMMERCE
National Technical Information Service

PB-287 473

Turbulence Modeling Applied to Buoyant Plumes

Aeronautical Research Associates of Princeton, Inc, NJ

Prepared for

Environmental Sciences Research Lab, Research Triangle Park, NC

Aug 78

United States
Environmental Protection
Agency

Environmental Sciences Research
Laboratory
Research Triangle Park NC 27711

EPA-600/4-78-050
August 1978

PB 287473

Research and Development

EPA

Turbulence Modeling Applied to Buoyant Plumes

REPRODUCED BY
NATIONAL TECHNICAL
INFORMATION SERVICE
U.S. DEPARTMENT OF COMMERCE
SPRINGFIELD, VA. 22161

57

TECHNICAL REPORT DATA *(Please read Instructions on the reverse before completing)*		
1. REPORT NO. EPA-600/4-78-050	2.	3. RECIPIENT'S ACCESSION NO. PB287473
4. TITLE AND SUBTITLE TURBULENCE MODELING APPLIED TO BUOYANT PLUMES		5. REPORT DATE August 1978 6. PERFORMING ORGANIZATION CODE
7. AUTHOR(S) M.L. Teske, W.S. Lewellen, and H.S. Segur		8. PERFORMING ORGANIZATION REPORT NO.
9. PERFORMING ORGANIZATION NAME AND ADDRESS Aeronautical Research Associates of Princeton, Inc. 50 Washington Road Princeton, New Jersey 08540		10. PROGRAM ELEMENT NO. 1AA601 CA-31 (FY-78) 11. CONTRACT/GRANT NO. 68-02-2285
12. SPONSORING AGENCY NAME AND ADDRESS Environmental Sciences Research Laboratory - RTP, NC Office of Research and Development U.S. Environmental Protection Agency Research Triangle Park, North Carolina 27711		13. TYPE OF REPORT AND PERIOD COVERED Interim 6/76 - 6/77 14. SPONSORING AGENCY CODE EPA/600/09
15. SUPPLEMENTARY NOTES		

16. ABSTRACT

A viable computer model was developed that is based on second-order closure of the turbulent correlation equations for predicting the fate of nonchemically reacting contaminants released in the atmospheric boundary layer. The invariant turbulence model discussed in previous reports has been extended to compute the development of buoyant plumes. Numerical program capability has been extended by improving the speed and accuracy of the two-dimensional unsteady turbulent flow calculation. Plume calculations are made for buoyant plumes rising into a stable quiescent atmosphere and stable, neutral, and unstable moving atmospheres. An examination of the application of an integral approach to our turbulent boundary layer model is also included.

17. KEY WORDS AND DOCUMENT ANALYSIS

a. DESCRIPTORS	b. IDENTIFIERS/OPEN ENDED TERMS	c. COSATI Field/Group
*Air pollution *Meteorology *Turbulence *Turbulent flow *Atmospheric diffusion *Mathematical Models		13B 04B 20D 04A 12A

18. DISTRIBUTION STATEMENT	19. SECURITY CLASS *(This Report)*	21. NO. OF PAGES
RELEASE TO PUBLIC	UNCLASSIFIED	57
	20. SECURITY CLASS *(This page)* UNCLASSIFIED	22. PRICE MF A01 PC A04

EPA Form 2220-1 (9-73)

EPA-600/4-78-050
August 1978

TURBULENCE MODELING APPLIED TO BUOYANT PLUMES

by

M. E. Teske, W. S. Lewellen, and H. S. Segur
Aeronautical Research Associates of Princeton, Inc.
Princeton, New Jersey 08540

Contract No. 68-02-2285

Project Officer

Francis S. Binkowski
Meteorology and Assessment Division
Environmental Sciences Research Laboratory
Research Triangle Park, North Carolina 27711

ENVIRONMENTAL SCIENCES RESEARCH LABORATORY
OFFICE OF RESEARCH AND DEVELOPMENT
U.S. ENVIRONMENTAL PROTECTION AGENCY
RESEARCH TRIANGLE PARK, NORTH CAROLINA 27711

DISCLAIMER

This report has been reviewed by the Environmental Sciences Research Laboratory, U.S. Environmental Protection Agency, and approved for publication. Approval does not signify that the contents necessarily reflect the views and policies of the U.S. Environmental Protection Agency, nor does mention of trade names or commercial products constitute endorsement or recommendation for use.

ABSTRACT

This report details the progress made at A.R.A.P. between March 1976 and April 1977 towards the goal of developing a viable computer model based on second-order closure of the turbulent correlation equations for predicting the fate of nonchemically reacting contaminants released in the atmospheric boundary layer. The invariant turbulence model discussed in previous reports has been extended to compute the development of buoyant plumes. Numerical program capability has been extended by improving the speed and accuracy of the two-dimensional unsteady turbulent flow calculation. Plume calculations are made for buoyant plumes rising into a stable quiescent atmosphere and stable, neutral, and unstable moving atmospheres. An examination of the application of an integral approach to our turbulent boundary layer model is also included.

This report was submitted in partial fulfillment of Contract No. EPA-68-02-2285 by Aeronautical Research Associates of Princeton, Inc. under the sponsorship of the Environmental Protection Agency. This report covers a period from March 1976 to April 1977, and work was completed as of April, 1977.

CONTENTS

Abstract iii

Figures. vi

Abbreviations and Symbols. ix

1. Introduction. 1
2. Conclusions 3
3. Recommendations 4
4. Computer Code Improvements and Modifications. . . 5
5. Model Comparison With Two-Dimensional Jets and Plumes Into a Quiescent Neutral Fluid 9
6. Two-Dimensional Plume In a Moving Stream. 22
7. Buoyant Plume Rise Into a Stable Quiescent Atmosphere. 26
8. Plume Rise into Moving Atmospheres. 32
9. An Examination of an Integral Approach to Use in Regional Air Quality Models 37

References 44

Preceding page blank

FIGURES

Number		Page
1	Comparison of the predicted cross-sectional mean velocity profile in a two-dimensional self-similar jet with the experimental observations of Kotsovinos (19).	13
2	Comparison of the predicted cross-sectional mean temperature profile in a two-dimensional self-similar jet with the observations of Kotsovinos (19).	13
3	Comparison of the predicted cross-sectional profile of the streaming velocity variance in a two-dimensional self-similar jet. The observations are from Kotsovinos (19) and Davies, et al. (20)	14
4	Comparison of the predicted cross-sectional profile of the temperature variance in a two-dimensional self-similar jet. The observations are from Kotsovinos (19), Davies, et al. (20), and Uberoi and Singh (21)	14
5	Comparison of the predicted cross-sectional mean velocity profile in a two-dimensional self-similar plume with the experimental observations of Kotsovinos (19).	15
6	Comparison of the predicted cross-sectional mean temperature profile in a two-dimensional self-similar plume with the observations of Kotsovinos (19).	15
7	Comparison of the predicted cross-sectional profile of the streaming velocity variance in a two-dimensional self-similar plume with the observations of Kotsovinos (19).	17
8	Comparison of the predicted cross-sectional profile of the temperature variance in a two-dimensional self-similar plume with the observations of Kotsovinos (19).	17

Number		Page
9	Decay of the normalized buoyancy flux as a function of downstream distance for a jet transition to a plume (data from Kotsovinos and List (22)).	18
10	Growth of the local Richardson number as a function of downstream distance for a jet transition to a plume (data from Kotsovinos and List (22)).	18
11	Predicted variation of the entrainment coefficient in two-dimensional jets and plumes compared with the average observed values of Kotsovinos (19).	21
12	The experimental result of run 83 of Cederwall (24) for a vertical buoyant slot jet exiting into a cross stream. The box size is our simulation region	24
13	An intensity plot of the variation of jet temperature within the box defined in Figure 12 for the Cederwall experiment. Maximum intensity corresponded to maximum temperature.	25
14	Prediction of the development of a rising plume into a quiescent stable atmosphere. Shown here are the contour lines at several times after flow initialization for the $q^2 = 0.7\ m^2/s^2$ value of turbulent kinetic energy.	29
15	Prediction of the development of a rising plume into a quiescent stable atmosphere. Shown here are various stream-function contours at several times after flow initialization.	30
16	Prediction of the downstream development of a moving buoyant plume into a stable atmosphere. Shown here are various passive tracer (smoke) contours at several distances downwind of the initialization plane.	35

Number		Page
17	Buoyant plume centerline rise height as a function of distance downstream of release point. Curves show the effects of unstable, neutral, and stable background temperature gradients. $\Delta\theta_{max}$ is the maximum difference between the initial plume temperature and the local ambient atmospheric temperature	36
18	Surface shear velocity as a function of Rossby number in a steady neutral planetary boundary layer. The exact solution is found from a solution of the partial differential equations of motion; the two dashed curves represent the results of our simplified integral theory. The decay parameter (1 or 0.2) multiplies the assumed exponential behavior of q in Equation 54.	43
19	Surface windshear angle as a function of Rossby number for the same conditions as Figure 18.	43

LIST OF ABBREVIATIONS AND SYMBOLS

A,b,s,v_c,a	invariant model constants (0.75,0.125,1.8,0.3,0.65)
$a_1,a_2,a_3,a_4,\lambda,\beta$	integral model constants
c	phase speed
C	mean smoke (passive tracer) concentration level
D	diameter, or jet width
f	Coriolis parameter ($2\Omega \sin \phi$)
F	buoyancy flux
Fr	Froude number (Equation 31)
g	gravity
k	wave number
ℓ_c	distance between cars
m	momentum flux (Equation 18)
N	Brunt-Vaisala frequency (Equation 2)
q	square root of twice the turbulent kinetic energy
$\dot{Q}_r$	driving heat flux
r	radius
Ri	Richardson number (Equation 19)
Ro	Rossby number (U_g/fz_o)
t	time
u^*	surface shear stress velocity
U_g	geostrophic velocity
U_i	mean fluid velocity
U_∞	freestream velocity
$\overline{u_i u_j}$	velocity correlation ensemble average
$\overline{u_i \theta}$	heat flux correlation ensemble average
x_i	coordinate (x,y,z)
z_o	hydrodynamic roughness
$z_{.5}$	distance to where U falls to one-half its centerline value

α_e	entrainment coefficient
β	buoyancy flux (Equation 17)
η	vorticity
θ	mean temperature
$\overline{\theta^2}$	temperature correlation ensemble average
Λ	scale length
μ	mass flux (Equation 20)
ρ_o	density
ϕ	latitude
ψ	streamfunction
Ω	angular velocity

Subscripts:

B	background
max	maximum
o	initial or surface
r	reference height

SECTION 1

INTRODUCTION

A.R.A.P. has been developing a program under EPA sponsorship since 1971 for practical predictions of the dispersal of pollutants in the atmosphere based on a second-order closure model of turbulence. This work is detailed in a number of reports and publications (1-10) and together with the work of others (11-15) has led to the general recognition that second-order closure approaches to turbulent modeling have a distinct advantage in terms of general validity over first-order eddy viscosity approaches. "Turbulence Modeling and Its Application to Atmospheric Diffusion, Part II" (4) contains a critical review of the current status of our A.R.A.P. invariant model. It contains a detailed discussion of the modeled terms, the empirical determination of the model coefficients, validation tests, and sample applications. A number of different plume disperal calculations have been made (1-5).

Section 4 contains a discussion of the modifications implemented within our computer codes to permit computation of buoyant plume rise. Sections 5 through 8 contain the results of the major effort in this contract, that of examining the behavior of buoyant plumes using these codes. Section 5 contains a comparison with one-dimensional plumes and jets, showing how well our predictions compare with results from a careful laboratory experiment. Section 6 shows the results of a calculation of a one-dimensional buoyant plume released into an ambient stream. In Section 7, we study the characteristics of a plume rising into a stable quiescent atmosphere. This computation demonstrates the

interaction of the heated plume with the surrounding stable atmosphere, and shows the production of Brunt-Vaisala waves from the plume and the development of the turbulence within the plume itself.

In Section 8, we discuss plumes rising into stable, neutral, and unstable moving atmospheres. Here we show the cross-sectional appearance of the plume, and comment upon plume bifurcation, rise height, and entrainment.

Section 9 deals with the other major task of our contract: an examination of the feasibility of second-order closure in three-dimensional applications. We propose an integral model that holds the promise of permitting a two-dimensional, unsteady computer code to compute a three-dimensional, unsteady regional air quality problem reasonably well.

SECTION 2

CONCLUSIONS

The A.R.A.P. computer model for predicting the fate of non-chemically reacting pollutants released into the atmospheric boundary layer has been extended to compute the development of buoyant plumes.

The sample calculations confirm the laboratory observations that positive buoyancy increases the entrainment rate into a plume.

When a plume is released into a stable atmosphere, sample calculations suggest that approximately 10 percent of the plume's energy is converted into radiating internal waves.

Under certain conditions, a rising plume from a point source can divide into two distinct plumes due to the vortex pair generated by the interaction of the wind and the plume.

Finally, in a separate integral analysis, we demonstrate a promising means of incorporating some of the capability of second-order closure modeling in the fully three-dimensional, unsteady case required for urban air quality models without going to a costly, fully three-dimensional code.

SECTION 3

RECOMMENDATIONS

The ultimate goal of this research is to permit the full power of the second-order closure approach to turbulent modeling to be applied to practical regional air quality models. One approach is to use individual plume predictions for a number of different combinations of atmospheric and release conditions to parameterize required modifications in the Gaussian plume distributions primarily used in air quality models. We believe such individual plume calculations as we have detailed in this report and in references 1-5 should be continued to utilize our model's current capabilities. However, computational efficiency may be achieved by vertically integrating the basic equations across the boundary layer. We then reduce the general problem to a two-dimensional, unsteady calculation for engineering estimates of the boundary-layer-averaged wind velocities and accompanying pollutant dispersal. The potential advantage in both accuracy and computer time over fully three-dimensional simulations based on first-order eddy viscosity approaches justifies pursuing the approach further.

SECTION 4

COMPUTER CODE IMPROVEMENTS AND MODIFICATIONS

A major effort of this past year was directed toward enhancing the two-dimensional, unsteady code developed over the last few years for the EPA, the Navy, and NASA to enable us to accurately compute plumes with significant vertical momentum. The most significant improvement came after our attempts at studying two-dimensional planetary boundary layers, particularly in a coastal environment (16). With a primitive equation code, using the hydrostatic pressure approximation and solving for the U and V velocities using their partial differential equations, we used a quadrature of the continuity equation to determine W , and therefore were forced to relax one boundary condition on W . Ideally, in this problem, we could anticipate that W approaches zero at the surface and at the top of the computational domain. Only one of these conditions could be used, and we had to permit flow through the top of the domain, since we needed W approaching zero at the surface. If we relax the hydrostatic approximation and include a dynamic equation for W , we are permitted both boundary conditions on W . However, we also had to include a loop to solve for the local pressure value. Fortunately, the solution of the Poisson equation in two dimensions has been explored carefully, and several reliable direct solution techniques are available for obtaining rapid results (17,18). However, the satisfaction of continuity (not an *a priori* assumption) had to be maintained by the addition of a correction term to the pressure forcing function. This technique was not always successful.

This problem is intensified whenever the hydrostatic pressure forms a dominant share of the pressure field. Then two terms (the vertical pressure gradient and temperature terms) tend to balance in the vertical momentum equation. The smallness of the remaining terms which determine W leads to excessive demands on the numerical accuracy.

In order to make the same program operational whether the hydrostatic approximation is valid or not, we recase our equations with streamfunction and vorticity as dependent variables. By defining $V = -\frac{\partial \psi}{\partial z}$ and $W = +\frac{\partial \psi}{\partial y}$, so that,

$$\nabla^2 \psi = -\left(\frac{\partial V}{\partial z} - \frac{\partial W}{\partial y}\right) = -\eta \qquad \text{(Eq. 1)}$$

we obtain an equation for η that does not contain the pressure. By discarding the imbalance problem, we do however acquire the difficulty of having to specify boundary conditions on ψ and η rather than V and W.

While we were modifying the code, we decided to gain some numerical accuracy in our implicit scheme by going to a Crank-Nicolson form of the tridiagonal matrix elements. This improvement, coupled with the streamfunction-vorticity formulation and the use of a generalized direct solver (now for ψ), have made significant improvements to our speed of computation (on the order of a 40 percent increase on our in-house computer) and the accuracy of the results. The computations discussed in Sections 7 through 9 were made with the enhanced version of the two-dimensional, unsteady code.

One of the major areas of concern, buoyant plume rise in a stable layer, forced us to study and handle the internal wave radiating boundary problem. Here a rising buoyant plume will radiate waves at frequencies that do not exceed the Brunt-Vaisala frequency

$$N = \left(\frac{g}{\theta_o} \frac{\partial \theta_B}{\partial z}\right)^{1/2} \qquad \text{(Eq. 2)}$$

These waves are constantly produced and tend to travel along the inversion, eventually reaching the boundary of our computational domain. In addition, the later stages of plume development see the propagation of waves of smaller and smaller wavelength. As the simulation proceeds, the computational mesh spacing becomes too large to resolve the wave structure. Either one or both of these problems may cause premature program termination by an inadequacy in our matching outflow boundary conditions or our mesh descretization.

At large horizontal distances from the source of the disturbances, the streamfunction, vorticity, and temperature each obey a wave radiation condition of the form

$$\frac{\partial \psi}{\partial t} + c \frac{\partial \psi}{\partial x} = 0 \quad , \qquad \text{(Eq. 3)}$$

where c is the linearized horizontal phase speed of the locally dominant wave,

$$c = N\sqrt{\frac{\psi}{\eta r^p}} \quad , \quad p = \begin{cases} 0 & \text{Cartesian} \\ 1 & \text{axisymmetric} \end{cases} \qquad \text{(Eq. 4)}$$

and we use the local values of ψ and η . A stable finite difference form of Equation 3 is

$$\psi_{n,t} - \psi_{n,t-1} + c \frac{\Delta t}{\Delta x} (\psi_{n,t} - \psi_{n-1,t-1}) = 0 \qquad \text{(Eq. 5)}$$

Similar conditions also hold for the vorticity and temperature. Since the dominant waves are inviscid, a simple zero slope at large x is sufficient for all turbulent correlations. These conditions appear to permit the smooth passage of Brunt-Vaisala waves through the outer boundary.

The mesh spacing near the plume centerline, however, is a more difficult problem. In this regard, we are constrained by a maximum possible number of mesh points, plus an empirical rule regarding the ratio of the maximum to mimimum spacing difference. Our algorithm for determining the streamfunction appears to set restrictions on the neighbor-to-neighbor spacing, $\Delta x_n / \Delta x_{n-1}$, or

on the maximum to minimum spacing, $\Delta x_{max}/\Delta x_{min}$. The precise limits have not yet been determined.

Documented versions of our one-dimensional boundary layer code and our two-dimensional pollutant dispersal code were delivered early in the contract period to our EPA technical monitor. A version of the full atmospheric code, containing the improvements discussed above, is currently being tested on the EPA Univac 1110.

SECTION 5

MODEL COMPARISON WITH TWO-DIMENSIONAL JETS AND PLUMES INTO A QUIESCENT NEUTRAL FLUID

Reliable atmospheric plume data taken under carefully controlled conditions are difficult to obtain. In this section, we compare model results with data on two-dimensional jets and plumes from controlled laboratory flows.

As long as the jet or plume has a parabolic character, it is possible to compute it using our one-dimensional code modified to permit a gravity component in the direction counter to the flow. As was done with the jet flows, we recast the equations into stream-line coordinates, avoiding the problem of computing the normal velocity W by defining the independent variable ψ as

$$\frac{\partial \psi}{\partial z} = U \qquad \text{(Eq. 6)}$$

and write the equations in their two-dimensional, steady version (marching downstream in x while solving for the one-dimensional variations in z). In these equations we assume that gravity now acts against the flow, so that in Donaldson's formulation the gravity vector is written as

$$g_i = (g, 0, 0)$$

The resulting equations for the mean streaming velocity and temperature, in the large Reynolds number limit, become

$$\frac{\partial U}{\partial x} = -\frac{\partial \overline{uw}}{\partial \psi} + \frac{g}{\theta_o}\frac{\theta}{U} \qquad \text{(Eq. 7)}$$

$$\frac{\partial \Theta}{\partial x} = -\frac{\partial \overline{w\theta}}{\partial \psi} \qquad \text{(Eq. 8)}$$

The appropriate Reynolds stress equations then become

$$\frac{\partial \overline{uw}}{\partial x} = -\overline{ww}\,\frac{\partial U}{\partial \psi} + \frac{g}{\theta_o}\,\frac{\overline{w\theta}}{U} + v_c\,\frac{\partial}{\partial \psi}\left(q\Lambda U\,\frac{\partial \overline{uw}}{\partial \psi}\right) - \frac{q}{\Lambda}\,\frac{\overline{uw}}{U} \qquad \text{(Eq. 9)}$$

$$\frac{\partial \overline{u\theta}}{\partial x} = -\overline{uw}\,\frac{\partial \Theta}{\partial \psi} - \overline{w\theta}\,\frac{\partial U}{\partial \psi} + \frac{g}{\theta_o}\,\frac{\overline{\theta^2}}{U} + v_c\,\frac{\partial}{\partial \psi}\left(q\Lambda U\,\frac{\partial \overline{u\theta}}{\partial \psi}\right) - \frac{qA}{\Lambda}\,\frac{\overline{u\theta}}{U} \qquad \text{(Eq. 10)}$$

$$\frac{\partial \overline{w\theta}}{\partial x} = -\overline{ww}\,\frac{\partial \Theta}{\partial \psi} + v_c\,\frac{\partial}{\partial \psi}\left(q\Lambda U\,\frac{\partial \overline{w\theta}}{\partial \psi}\right) - \frac{qA}{\Lambda}\,\frac{\overline{w\theta}}{U} \qquad \text{(Eq. 11)}$$

$$\frac{\partial \overline{\theta^2}}{\partial x} = -2\overline{w\theta}\,\frac{\partial \Theta}{\partial \psi} + v_c\,\frac{\partial}{\partial \psi}\left(q\Lambda U\,\frac{\partial \overline{\theta^2}}{\partial \psi}\right) - \frac{2bsq}{\Lambda}\,\frac{\overline{\theta^2}}{U} \qquad \text{(Eq. 12)}$$

$$\frac{\partial \overline{uu}}{\partial x} = -2\overline{uw}\,\frac{\partial U}{\partial \psi} + \frac{g}{\theta_o}\,\frac{\overline{u\theta}}{U} + v_c\,\frac{\partial}{\partial \psi}\left(q\Lambda U\,\frac{\partial \overline{uu}}{\partial \psi}\right) - \frac{q}{\Lambda U}\left(\overline{uu} - \tfrac{1}{3}q^2\right) - \frac{2bq^3}{3\Lambda U} \qquad \text{(Eq. 13)}$$

$$\frac{\partial \overline{vv}}{\partial x} = v_c\,\frac{\partial}{\partial \psi}\left(q\Lambda U\,\frac{\partial \overline{vv}}{\partial \psi}\right) - \frac{q}{\Lambda U}\left(\overline{vv} - \tfrac{1}{3}q^2\right) - \frac{2bq^3}{3\Lambda U} \qquad \text{(Eq. 14)}$$

$$\frac{\partial \overline{ww}}{\partial x} = v_c\,\frac{\partial}{\partial \psi}\left(q\Lambda U\,\frac{\partial \overline{ww}}{\partial \psi}\right) - \frac{q}{\Lambda U}\left(\overline{ww} - \tfrac{1}{3}q^2\right) - \frac{2bq^3}{3\Lambda U} \qquad \text{(Eq. 15)}$$

with the scale length given dynamically by the equation

$$\frac{\partial \Lambda}{\partial x} = 0.35\,\frac{\Lambda}{q^2}\,\overline{uw}\,\frac{\partial U}{\partial \psi} + 0.6\,\frac{bq}{U} + v_c\,\frac{\partial}{\partial \psi}\left(q\Lambda U\,\frac{\partial \Lambda}{\partial \psi}\right) - \frac{0.375U}{q}\left(\frac{\partial q\Lambda}{\partial \psi}\right)^2 + \frac{0.8\Lambda}{q^2}\,\frac{g}{\theta_o}\,\overline{u\theta} \qquad \text{(Eq. 16)}$$

When $g = 0$ these equations may be used to compute a two-dimensional jet and the transition to a plume obtained as g is increased.

Our prediction of the flow in a two-dimensional wake has been presented previously (4) and shows how well the model does (without the permission of model constant change) at predicting the deficit velocity, temperature, and turbulent correlation profiles in the self-similar region. Similar results for the two-dimensional jet are shown in Figures 1-4 and compared against available laboratory data (19-21). We begin our calculation with Gaussian distributions of velocity, temperature, and turbulence, and run until similarity exists. In his experiment, Kotsovinos exhausts heated water from a slot into a large quiescent water tank. Thermistors and a laser Doppler velocimeter permit him to determine the flowfield. In all cases, we show his furthest downstream results only; one of his experimental curves (his Figure 4.2.4) clearly shows that he has not yet reached similarity. Our numerical predictions show that his last station may be taken as a reasonable estimate of similarity, however.

Figures 1 and 2 show the normalized cross-sectional profiles of streaming velocity and temperature. All curves are plotted normalized by the half-width of the velocity profile (as appropriate from the experiment or the prediction). These figures show that our model does a reasonable job of predicting the mean profiles, although one would like better agreement at the larger z distances. These curves will be discussed in greater detail later.

Figures 3 and 4 give the similarity profiles of the variance of the velocity in the streaming direction, $\sqrt{\overline{uu}}$, and the temperature $\sqrt{\overline{\theta^2}}$. Both predictions fall within the scatter of the data and tend to tail out a little high near the edges of the jet. Our results for these same model constants in the two-dimensional wake overpredicted the behavior of $\overline{\theta^2}$. A modification of the constants to improve the prediction in one case would probably worsen the prediction in the other. The predicted mean profiles

do not fall off as rapidly as the data suggest. The reasons for this behavior are unclear, but may involve the numerical approach used to solve for the expanding jet, a technique in streamfunction coordinates that requires $U_{edge} > 0$.

Kotsovinos also studied the two-dimensional plume by heating his exiting water to a high enough level to permit gravity to influence the development of the flow. In this way, he was able to arrive at the entrainment properties of the simple plume; our comparisons with his results are given in Figures 5-8.

Figure 5 shows the good agreement we obtain with the mean velocity profile. In fact, in the normalized units plotted here, our predictions for U for both the jet and the plume are nearly identical. The one difference not seen from this plot is that U_{max} in both experiments and predictions in the jet are decaying as $(x/D)^{-1/2}$, while the plume value reaches a fixed, constant value of $U_{max}/U_{max_o} = 1.1$. The spread rate $\Delta z_{.5}/\Delta x$ grows at a slope of 0.13 for the plume and 0.12 for the jet, both consistent with the experiments.

In Figure 6, we show a disappointing comparison with the mean temperature measurements. Here we underpredict the plume profiles, while we tended to overpredict the jet profiles. Before we begin questioning the model, however, it is best to note that we are using the same model constants to predict three types of two-dimensional flows: jets, wakes, and plumes. Gravity definitely affects the cross-sectional temperature profile, yet the similarity between the plume and jet predictions still exists. A plot of the behavior of the maximum temperature as a function of downstream distance shows that in the experiment the jet temperature falls asymptotically as $0.28(x/D)^{-1/2}$ while the plume decays as $0.28(x/D)^{-1}$. Our simulation gives $0.34(x/D)^{-1/2}$ for the jet, and $0.32(x/D)^{-1}$ for the plume.

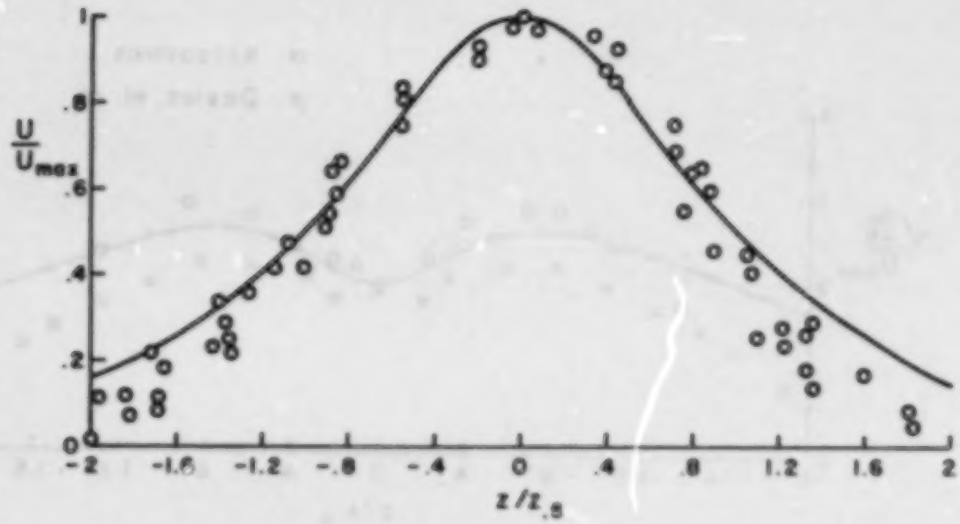

Figure 1. Comparison of the predicted cross-sectional mean velocity profile in a two-dimensional self-semilar jet with the experimental observations of Kotsovinos (19).

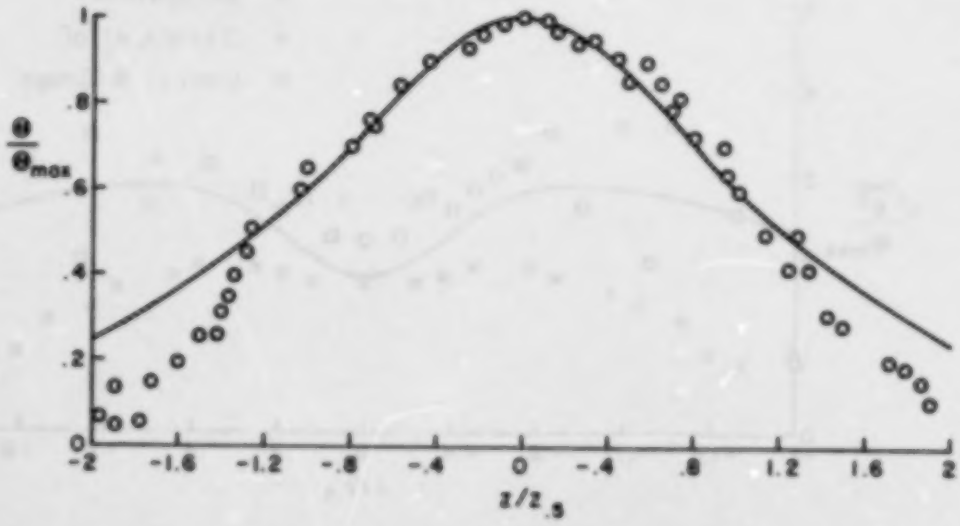

Figure 2. Comparison of the predicted cross-sectional mean temperature profile in a two-dimensional self-similar jet with the observations of Kotsovinos (19).

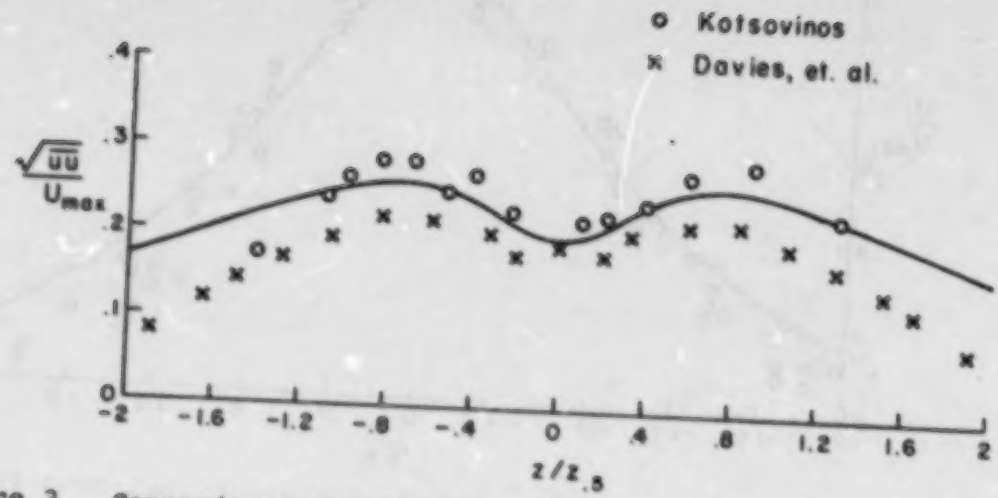

Figure 3. Comparison of the predicted cross-sectional profile of the streaming velocity variance in a two-dimensional self-similar jet. The observations are from Kotsovinos (19) and Davies, et al. (20).

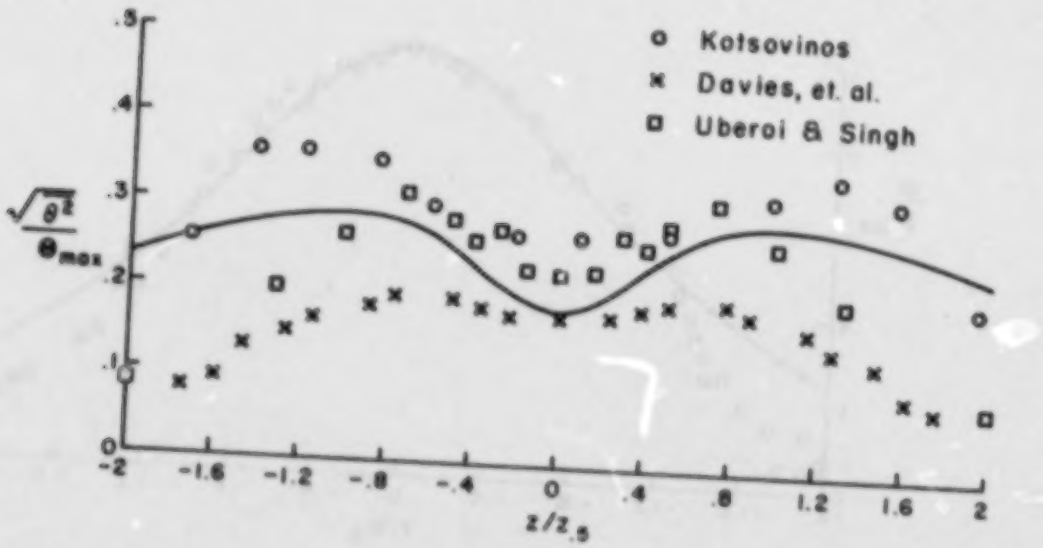

Figure 4. Comparison of the predicted cross-sectional profile of the temperature variance in a two-dimensional self-similar jet. The observations are from Kotsovinos (19), Davies, et al. (20), and Uberoi and Singh (21).

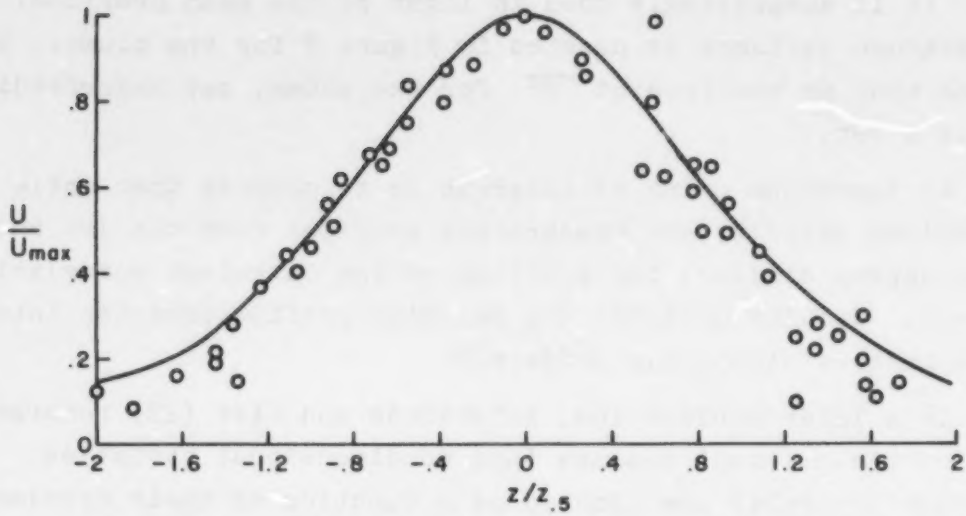

Figure 5. Comparison of the predicted cross-sectional mean velocity profile in a two-dimensional self-similar plume with the experimental observations of Kotsovinos (19).

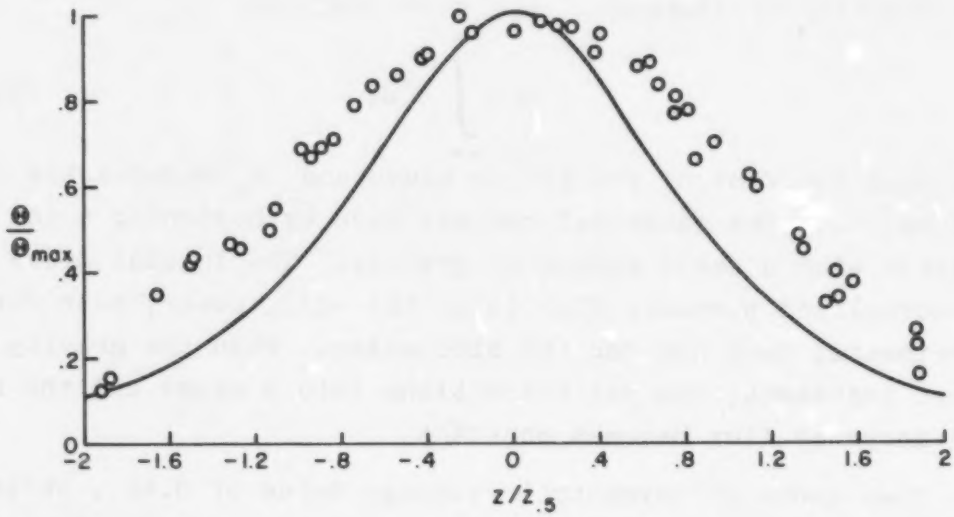

Figure 6. Comparison of the predicted cross-sectional mean temperature profile in a two-dimensional self-similar plume with the observations of Kotsovinos (19).

Figure 7 shows a comparison of the velocity correlation $\overline{uu}$. It is surprisingly good in light of the mean profiles. The temperature variance is plotted in Figure 8 for the plume. Now we see that we overpredict $\overline{\theta^2}$ for the plume, but underpredict it for a jet.

An important point of interest is to observe that while the normalized velocity and temperature profiles from the jet and the plume appear similar, the profiles of the turbulent correlations are not. Gravity modifies the jet-like profile behavior into a shape that is distinctly different.

In a later publication, Kotsovinos and List (22) reworked some of the original results into nondimensional variables. Two of these variables are plotted as a function of their nondimensional downstream distance in Figures 9 and 10. In Figure 9 we show the variation of the buoyancy flux

$$\beta = \frac{g}{\theta_o}\int_{-\infty}^{\infty} U\theta dz \qquad \text{(Eq. 17)}$$

as a function of distance. (In these figures,

$$m = \int_{-\infty}^{\infty} U^2 dz \qquad \text{(Eq. 18)}$$

is a momentum flux of the jet or plume and m_o denotes the initial value.) The numerical run was made by beginning a jet calculation with a small amount of gravity. The initial decay of the normalized buoyancy flux is at the -1/2, power, both for the experimental data and for the simulation. When the gravity effect increases, the jet transitions into a plume and the normalized buoyancy flux becomes constant.

They quote an asympototic average value of 0.42 , while we obtain 0.33 .

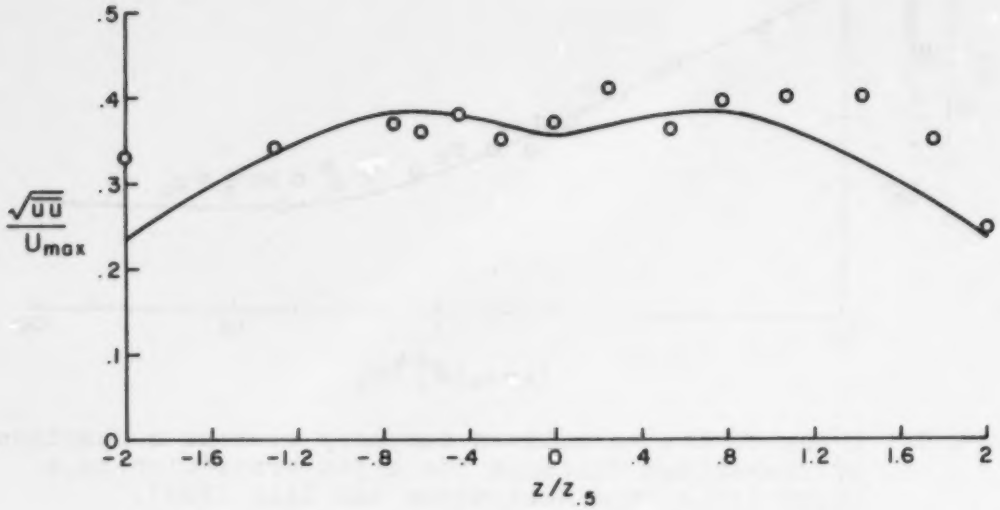

Figure 7. Comparison of the predicted cross-sectional profile of the streaming velocity variance in a two-dimensional self-similar plume with the observations of Kotsovinos (19).

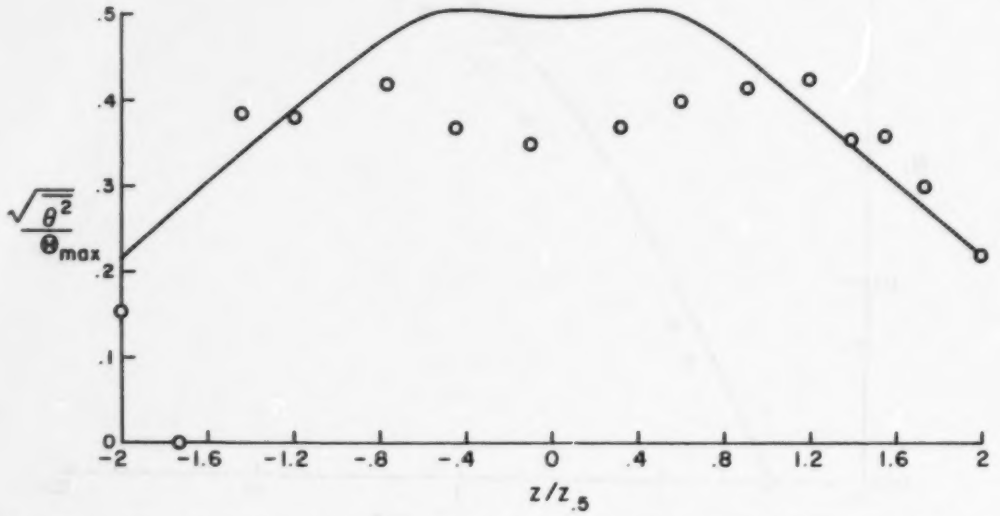

Figure 8. Comparison of the predicted cross-sectional profile of the temperature variance in a two-dimensional self-similar plume with the observations of Kotsovinos (19).

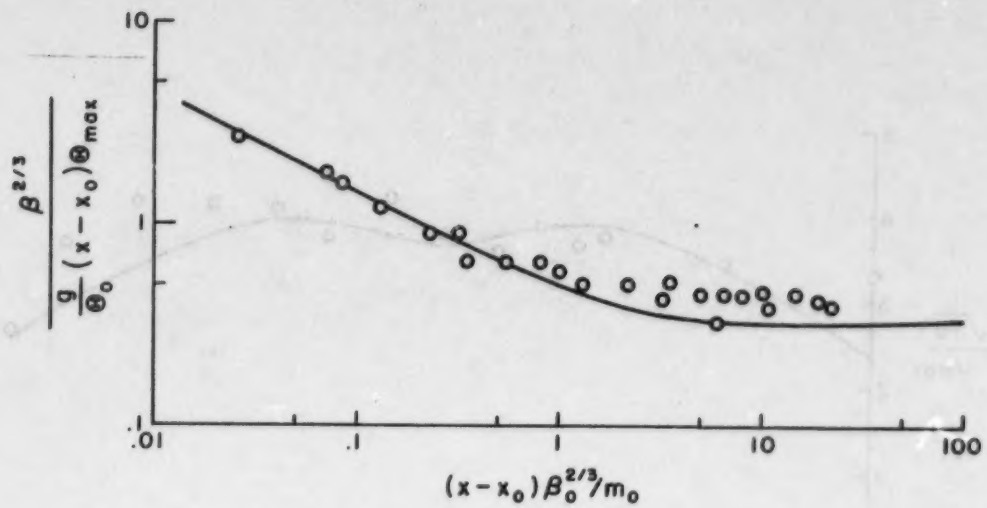

Figure 9. Decay of the normalized buoyancy flux as a function of downstream distance for a jet transition to a plume (data from Kotsovinos and list (22)).

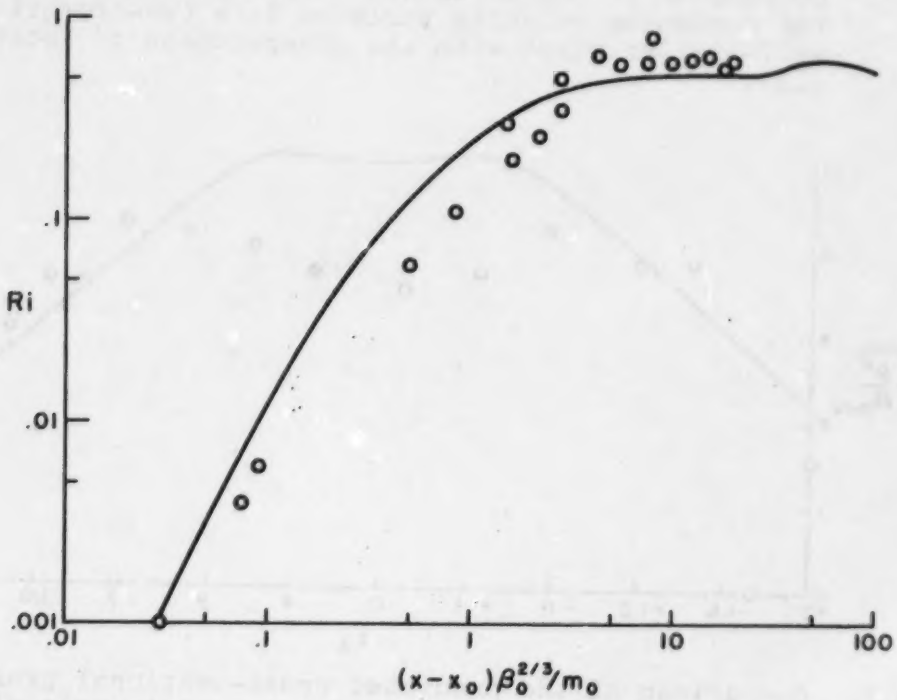

Figure 10. Growth of the local Richardson number as a function of downstream distance for a jet transition to a plume (data from Kotsovinos and List (22)).

In Figure 10, we compare the predicted and observed behavior of the local Richardson number,

$$Ri = \frac{\mu^3 \beta}{m^3} \qquad \text{(Eq. 19)}$$

Where

$$\mu = \int_{-\infty}^{\infty} U dz \qquad \text{(Eq. 20)}$$

is the mass flux. The predicted initial growth of Ri is at the 3/2 power, consistent with the experimental observations. The predicted values typically exceed the experimental data at intermediate distances; but eventually oscillate about a mean quite close to the observed value of 0.63 . Both of these curves show a favorable comparison between numerical predictions and experimental observations.

The biggest discrepancy between the data of Kotsovinos and List, and our predictions, is in their plot of the mass-to-momentum ratio

$$C = \frac{\mu}{[m(x-x_o)]^{1/2}} \qquad \text{(Eq. 21)}$$

They demonstrate that C may be taken at a constant value of 0.54 throughout the jet-to-plume transition. Our simulation is consistent with a constant, also, but at a higher value of C = 0.70.

An interesting feature of the predictions is the variation in the entrainment coefficient αe , for both the jet and the plume, where αe is defined as

$$\alpha_e = \frac{\partial Q}{\partial x} \qquad \text{(Eq. 22)}$$

with Q the mass flux in the x direction, measured along the centerline. In Figure 11, we plot αe for both the jet and the

plume. The predicted asympototic behavior for the jet is $\alpha_e = 0.042$, while for the plume we obtain $\alpha_e = 0.115$. These values may be compared with the observed averaged values quoted by Kotsovinos, $\alpha_e = 0.055$ for the jet and 0.11 for the plume over the approximate duration of his experiments. The predicted similarity value for plume entrainment is within 5 percent of his average values, but is only within 13 percent for jet entrainment at $x/D = 200$. In their later publication, Kotsovinos and List (22) note that a constant entrainment coefficient does not describe their experimental measurements as well as the constant C. Further comparison may be made with Briggs (23), who cites three-dimensional values of 0.090 for the jet and 0.125 for the plume.

The largest uncertainty in the model itself is the edge boundary condition on the dynamic scale. A fine tuning of this condition from a value which gives good agreement in the two-dimensional wake (10) to a 25 percent higher value would raise the asymptotic value of the jet entrainment to 0.055 . However, we have not considered such fine tuning as justified at the present time.

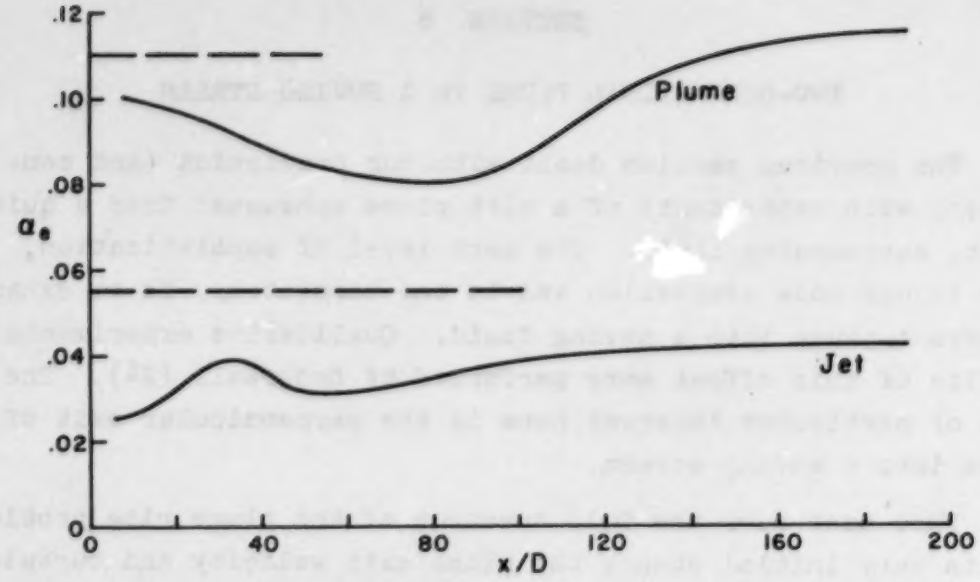

Figure 11. Predicted variation of the entrainment coefficient in two-dimensional jets and plumes compared with the average observed values of Kotsovinos (19).

SECTION 6

TWO-DIMENSIONAL PLUME IN A MOVING STREAM

The previous section dealt with our prediction (and comparison with experiment) of a slot plume exhausted into a quiescent, surrounding fluid. The next level of sophistication, both in our code simulation and in the laboratory, is to exhaust a buoyant plume into a moving fluid. Qualitative experimental results of this effect were performed by Cederwall (24). The case of particular interest here is the perpendicular exit of a plume into a moving stream.

This case runs the full spectrum of the plume rise problem. In its very initial stages the plume exit velocity and turbulence dominate the problem, and the plume continued rising from its source without influence from the ambient crosswind. Eventually, however, the flowing stream forces the plume to begin bending over; it naturally continues to spread during this process, and would continue to rise (however slightly) unless its vertical movement is capped by a temperature inversion. In the laboratory configuration, the plume spreads until it penetrates the entire streaming depth.

If we confine our attention to a single experimental run - one shown visually as exiting normal to the freestream (his run 83) - then all of the necessary data are available to simulate the experimental setup. In this particular case, the jet was flowing at 17 times the speed of the freestream cross-flow; the source Froude number was set to 0.57 (this, with an assumption on the shape of the exiting jet and the freestream speed, permits the evaluation of the temperature difference between jet and

ambient fluid); and the normalized volume flux was 23 (giving the needed fluid depth to balance the exiting jet flow volume). Figure 12 shows the experimental run of Cederwall for this particular case.

To shorten the computer time to reach steady state, we confine our attention to the superimposed box region as shown in Figure 12. Within this region, we assume that the incoming uniform stream (from the left) enters at $V = 4$ m/sec , to interact with an exiting slot jet of the form

$$W_{jet} = W_{max} \exp(-(y/D)^2) \qquad \text{(Eq. 23)}$$

with $W_{max} = 17$ and $D = 1$. We assume that the exit temperature may be represented by a Gaussian distribution with $\theta_{max} = 1.8°C$ (consistent with the experimental source Froude number).

For this simulation we need to assume a jet turbulence level. From Kotsovino's work in the last section (and Figure 3), we see that the streaming correlation may reach a value of $\sqrt{\overline{ww}}/W_{max} = 0.3$. Assuming that this constitutes half of the turbulence level, we set the maximum $q^2 = 50$ m^2/sec^2 , also in a Gaussian distribution with $D = 1$.

At the jet exit (the lower boundary), the equation for W_{jet} may be integrated and differentiated to give the lower boundary conditions on ψ and η , respectively. The freestream inflow vorticity is assumed equal to zero, while the inflow ψ is consistent with the uniform inflow. Along the top ψ is held at its maximum inflow value, and $\eta = 0$. A zero slope condition is imposed on ψ along the outflow boundary. The temperature and turbulence profiles are likewise assumed known along the lower and inflow boundaries, and are permitted zero slopes at the top and downstream boundaries.

Our simulation is shown in Figure 13. Qualitative comparison is quite good, with the general bending-over character of the exit slot jet clearly evident.

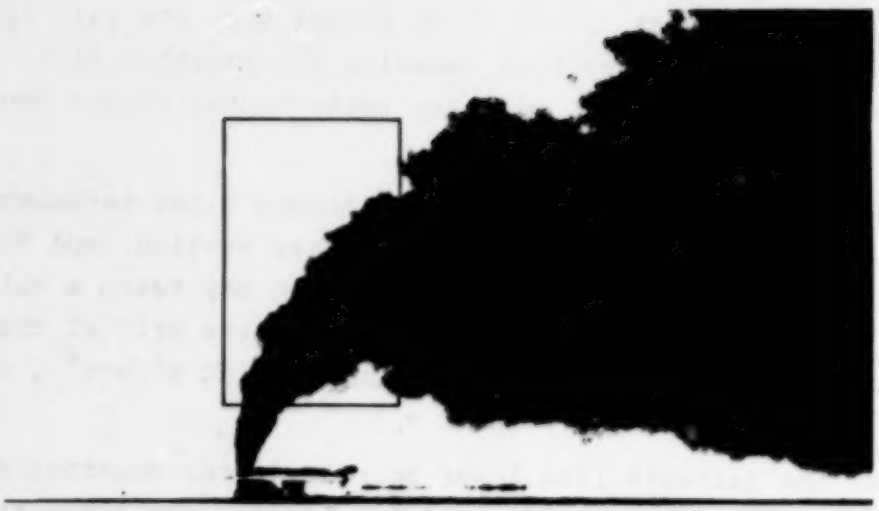

Figure 12. The experimental result of Cederwall's run 83 (24) for a vertical buoyant slot jet exiting into a cross-stream. The box size is our simulation region.

Figure 13. An intensity plot of the variation of jet temperature within the box defined in Figure 12 for the Cederwall experiment. Maximum intensity corresponds to maximum temperature.

SECTION 7

BUOYANT PLUME RISE INTO A STABLE QUIESCENT ATMOSPHERE

We next examine a two-dimensional, unsteady calculation of buoyant plume rise from a heated surface into a quiescent atmosphere. Here, we wish to study not only the time-development of the plume and the periodic character of the wave structure outside the plume, but also the effective interaction of the plume with the surface layer.

For this calculation, we use an axisymmetric version of the two-dimensional code developed under contract to the Nuclear Regulatory Commission to study strongly swirling flows. In the present case we are not interested in the swirl, but only in the radial coordinate system. We represent the stable atmosphere by a constant background temperature gradient $\partial\theta_B/\partial z$ of 0.003°C/m. Along the lower surface we assume that the flow is sufficiently unstable so that the surface will be free-convection-like (8) at a reference height of $z_r = 1$ m above a hydrodynamic roughness height of $z_o = 0.1$ m. In this case, we may set $\psi = 0$ at z_r. The vorticity carries a compatibility relationship to the streamfunction through the Poisson equation, which reduces to the form

$$\eta = -\frac{2\psi_+}{(\Delta z)^2\left[1 + \frac{2z\ \ln(z/z_o)}{\Delta z}\right]} \qquad \text{(Eq. 24)}$$

where ψ_+ is the streamfunction value at the point above z_r.

The presence of a heated surface is felt by assuming that the temperature at z_o is a simple Gaussian distribution of 3°C

maximum value and 100°m spread. The wide spread is suggestive of cooling tower dimensions; a surface temperature assumed no larger than the stable temperature at the top of the computational domain (at 1000 m) ensures that the developing plume will be capped within our field of interest. The temperature at z_r is then given by formula

$$\theta_r = \theta_s + (\theta_+ - \theta_s) \frac{(z_r^{-1/3} - z_o^{-1/3})}{(z_+^{-1/3} - z_o^{-1/3})} \qquad \text{(Eq. 25)}$$

where θ_+ is the temperature at $z_+ > z_r$, and θ_s is the surface temperature.

We anticipate that as the plume develops, it will entrain fluid from along the surface and accelerate it into the unstable layer near the origin. The presence of the ambient stable temperature gradient permits the development of Brunt-Vaisala waves above the plume. These waves will interact with the far-field boundaries, and will also lead to the radiation of waves of smaller and smaller wavelengths. Our radiating boundary condition, discussed in Section 5, will handle the far-field conditions; however, the short wavelength waves will eventually become too small to be defined by the mesh spacing near $r = 0$.

An illustration of the plume buildup and oscillation may be observed in Figure 14 where we have plotted a near-edge coutour value of the turbulent kinetic energy q^2, its $0.1\ m^2/s^2$ value. Starting from nominally zero values, the plume had reached an altitude of nearly 200 meters and a radial spread of 100 meters by a time of 300 seconds. The continued upward movement of the plume is arrested near $t = 600$ seconds, after which time the top of it drops. At this time, the first internal gravity wave is generated. Further time slots show the movement of the top of the plume and the regular (almost steady) profile to the plume below 100 meters. The top of the plume is located near

330 meters. The rise height in a calm, stable atmosphere may be estimated from a formula given by Briggs (23)

$$\Delta z = 5.0\, F^{1/4}\, N^{-3/4} \qquad \text{(Eq. 26)}$$

where the buoyancy flux is given by

$$F = \frac{1}{\pi}\frac{g}{\theta_o}\iint (W\theta+\overline{w\theta})dA \qquad \text{(Eq. 27)}$$

Evaluating these formulas at the reference height, we find that the rise height of the plume should be about 300 meters. Thus, it would appear as though the early time behavior of the simulation is quite consistent with available observations.

The nature of the radiating wave patterns may be seen by presenting the streamline patterns at several times (Figure 15). Figure 15a gives the pattern at t = 300 seconds, when the simple structure is a vortex ring (i.e., at one-half of a Brunt-Vaisala period, the first internal gravity wave has been generated). By t = 600, Figure 15b, the ring is flattened slightly by a second ring (or wave) developing near z = 300 meters (where the top of the plume exists). By t = 900, the ring in Figure 15b has enveloped a large portion of the domain of observation, and a second ring of opposite sign has appeared above the plume. A new cell is just beginning near r = 0. The structure near z = 300 meters is quite complicated and exibits two vertical stagnation points at 300 and 350 meters. Subsequent frames show the continued pattern development. The streamline cell structure is now clearly visible, and we observe that the wave structure does not appear to have any problems in passing through the large radial boundary.

This is a sample of a plume problem where the application of a simple turbulent entrainment coefficient would be inappropriate. The low-level convergence due to the buoyant acceleration of the plume, and the upper-level divergence due to the negative buoyancy,

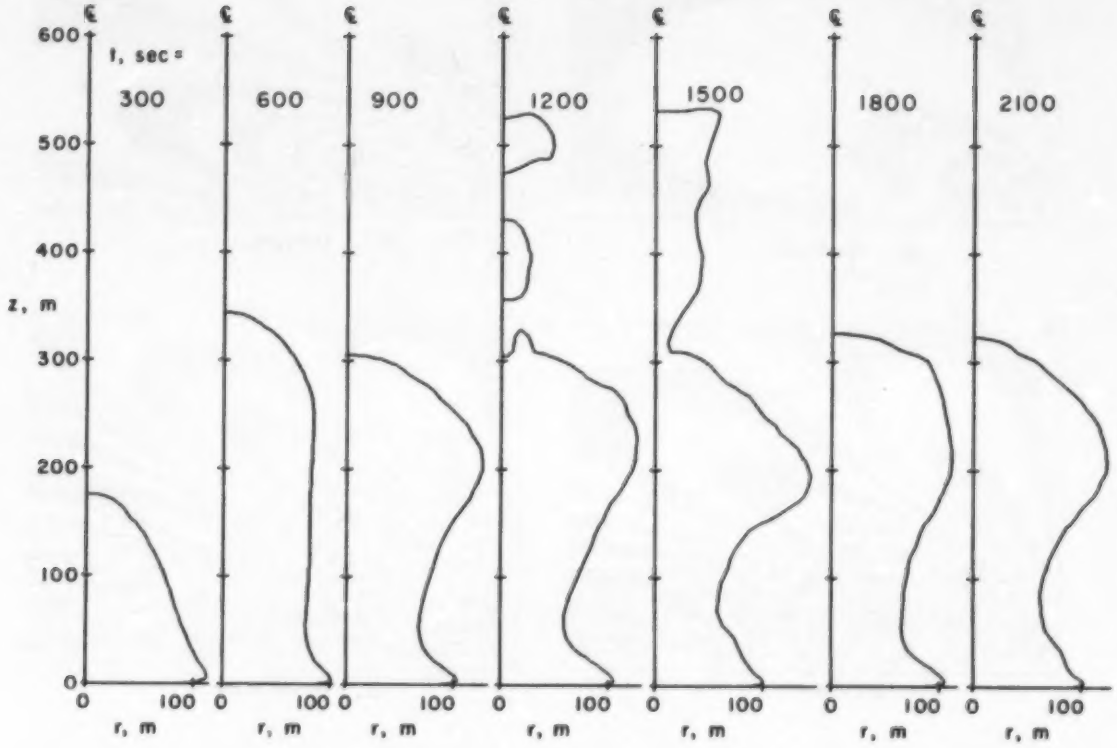

Figure 14. Prediction of the development of a rising plume into a quiescent stable atmosphere. Shown here are the contour lines at several times after flow initialization for the $q^2 = 0.1\ m^2/s^2$ value of turbulent kinetic energy.

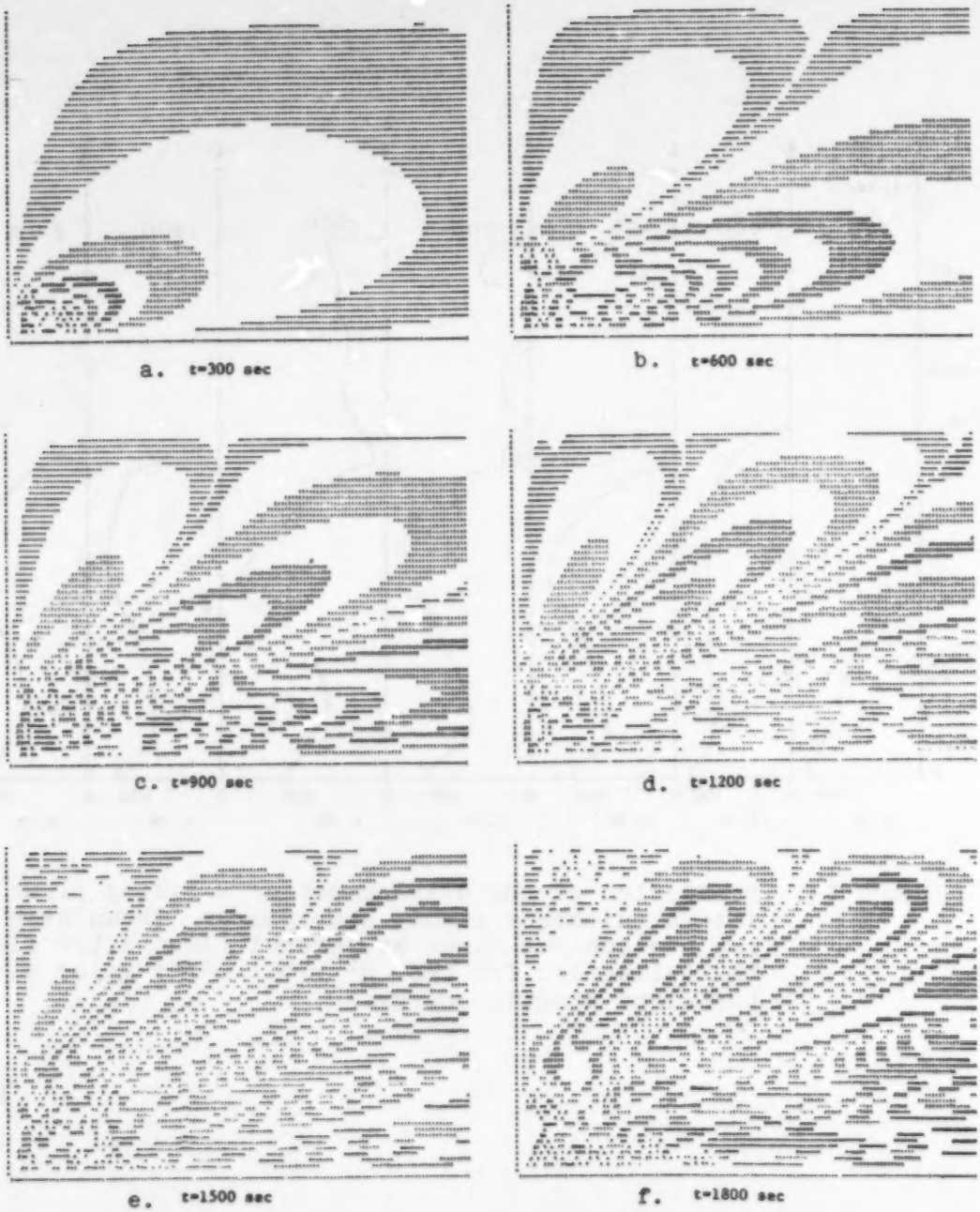

Figure 15. Prediction of the development of a rising plume into a quiescent stable atmosphere. Shown here are various streamfunction contours at several times after flow initialization.

are intimately connected with the turbulence, so that a simple turbulent entrainment cannot be separated from the rest of the flow mechanisms operating in the problem.

The rising plume establishes a complicated cross-sectional flow pattern into which the stable background temperature gradient permits the generation of Brunt-Vaisala waves. Surface heat flux drives the plume development, while the Brunt-Vaisala waves carry some energy from the plume (turbulent dissipation handles the rest). To estimate the significance of the waves as energy carriers, we compare the ratio of energy lost along the outflow boundary to the energy inflow at the surface. It may be shown that by linearizing the governing equations in the large r region, the average energy flux through the boundary may be written as

$$E_{out} = \pi\rho_o \int_{z_r}^{z_{max}} r_{max} \left\langle U^2 + W^2 + \left[\frac{N(\theta-\theta_B)}{\partial\theta_B/\partial z}\right]^2 \right\rangle \left\{\frac{Nz^2}{kr_{max}^2}\right\} dz \qquad \text{(Eq. 28)}$$

evaluated at $r = r_{max}$, where l is the wave number of the outgoing waves, $\{Nz^2/kr^2\}$ is the group velocity, and $\langle\cdot\rangle$ denotes the average over a wave period. This quantity is compared with the total turbulent heat flux coming through the surface

$$E_{in} = \frac{2\pi g\rho_o}{\theta_o(\partial\theta_B/\partial z)} \int_0^{r_{max}} r\theta\overline{w\theta}dr \qquad \text{(Eq. 29)}$$

evaluated at $z = z_o$. Using the results for $t > 1200$ seconds, we find that the energy carried away from the vicinity of the plume by the waves may amount to 10 percent of the entering energy. Over 70 percent of the energy is dissipated by turbulent kinetic energy processes within this same region. At larger radii, energy is lost from the waves to thermal dissipation of the potential energy.

SECTION 8

PLUME RISE INTO MOVING ATMOSPHERES

We now turn our attention to the corresponding plume rise problem in a moving atmosphere. We use the two-dimensional, unsteady code, marching in x downwind of the plume release point. This technique forces us to begin computation after the buoyant plume has become sufficiently bent-over that $(W/U_\infty)^2 << 1$. All of our calculations begin with a Gaussian distribution of the heated air. Our simulation tracks its behavior downstream, as it forces the formation of a vortex pair as it rises, entraining surrounding air, and producing turbulence.

A straightforward application of our work with aircraft vortex wakes leads to the solution for plumes rising in a neutral atmosphere. These results were presented at the AMS Third Symposium on Atmospheric Turbulence, Diffusion, and Air Quality (2). Our discussion will center primarily upon the behavior of the plumes emitted into moving stable atmospheres.

We again may begin with a Gaussian distribution of temperature at the assumed point of plume emission. In the initial development of the plume, we do not anticipate any appreciable interactions with the surface; thus, we use a simple no-slip boundary condition there. At large y distances, we use the two-dimenional analogue to Equation 5 for the radiating wave condition. We again begin with a background temperature gradient of $\partial\theta_B/\partial z = 0.003°C/meter$. For this simulation we are able to calculate the transport of a passive species, as well as the temperature and velocity components, and will use the tracer pro-

file behavior to illustrate the problem simulation.

Beginning with a simple Gaussian distribution for the tracer, we show in Figure 16 its later downstream development. Figure 16a shows the contour shapes x = 500 meters after initialization. The simple Gaussian structure with maximum value located at z = 200 meters and a spread of 65 meters has risen above z = 400 meters by this frame. The top of the plume is flattening out as the stable layer is penetrated. At x = 1000 meters, Figure 16b, the plume has continued diffusing upward and outward into the stable layer. Figure 16c shows that the plume is in a downward oscillation by x = 1500 meters, while the final frame, 16d, shows that the plume at x = 2000 meters is spreading laterally along the stable inversion layer. Cross-sectional profiles of the streamlines are very similar to those produced by the quiescent plume rise.

A formula from Briggs (23) for computing plume rise height for bent-over plumes in an atmosphere of constant stratification is

$$\Delta z = 2.6\left(\frac{F}{U_\infty N^2}\right)^{1/3} \qquad \text{(Eq. 30)}$$

where F has been defined in Equation 27. Substituting into Equation 30 with the data from this simulation, we find that $\Delta z \sim$ 260 meters. Inspecting the 2 percent contour on the tracer, we find that our simulation gives $\Delta z \sim$ 300 meters.

We may compare the rise height of the center of the plume rising into stable layers with the rise heights for neutral and unstable layers as shown in Figure 17. Normalization by the Froude number

$$Fr = \left[\frac{g}{\theta_o}\,\frac{\Delta\theta_{max}}{U_\infty^2}\,D\right]^{-1/2} \qquad \text{(Eq. 31)}$$

permits the collapse of all buoyant plumes released into neutral surroundings to the single solid curve shown, with the asymptote as given. Unstable layers accelerate the plume rise, while a stable layer will stop the plume rise. The oscillations about its inversion level are the Brunt-Vaisala waves.

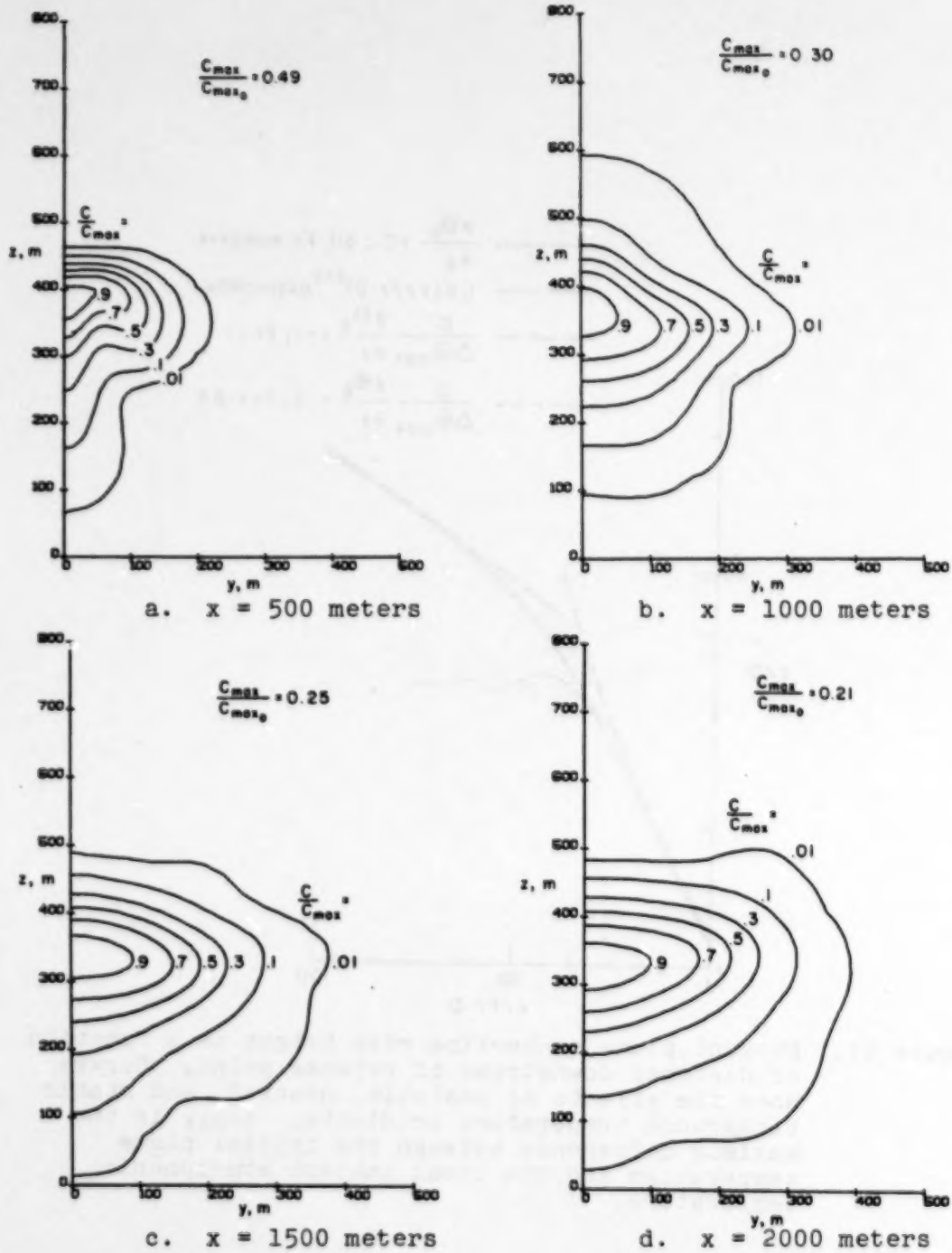

Figure 16. Prediction of the downstream development of a moving buoyant plume into a stable atmosphere. Shown here are various passive tracer (smoke) contours at several distances downwind of the initialization plane.

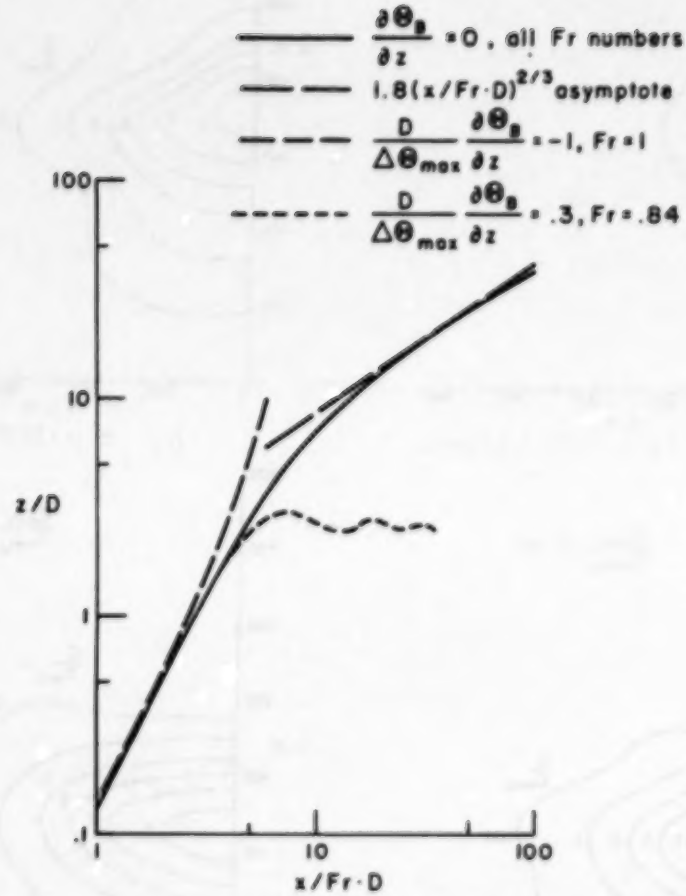

Figure 17. Buoyant plume centerline rise height as a function of distance downstream of release point. Curves show the effects of unstable, neutral, and stable background temperature gradients. $\Delta\theta_{max}$ is the maximum difference between the initial plume temperature and the local ambient atmospheric temperature.

SECTION 9

AN EXAMINATION OF AN INTEGRAL APPROACH TO USE IN REGIONAL AIR QUALITY MODELS

One of the tasks in the current contract is to identify how second-order closure may best be utilized in practical urban or regional air quality models involving complex terrain and numerous plumes. One way to utilize a sophisticated model is to use individual plume predictions for a number of different combinations of atmospheric and chimney exit conditions to parametrize modifications in the Gaussian plume distributions presently used in air quality models. We have made such calculations (1) and plan to continue this type of calculation in the future. However, it seems probable that in many situations the full influence of complicated terrain or unsteadiness cannot be parameterized on the basis of the individual steady plume calculations. It is possible to consider using the full model for direct three-dimensional, unsteady numerical calculations, but the enormous computing load this entails makes it highly desirable to seek some practical approximations.

We have experimented with vertically integrating the basic equations across the boundary layer to remove one dimension from the problem. This will reduce the general problem to a two-dimensional, unsteady calculation for the boundary-layer-averaged variables. The integration process is exact, but approximations must be introduced to parameterize the relationships between the different integrals which occur in order to close the set of equations. Results of a simple test of this approach indicate that it may be the best approach to follow to obtain a practical model for air quality studies.

To see how this process may work, we consider the limiting case of a neutral planetary boundary layer. The equations for the mean velocities and second-layer correlations as given in reference 4 may be integrated to yield

$$\frac{\partial \langle U_g - U \rangle}{\partial t} + \frac{\partial \langle U^2 - U^2 \rangle_g}{\partial x} - \frac{\partial \langle VU \rangle}{\partial y} + (WU)_o = -f\langle V \rangle - \overline{uw}_o \qquad \text{(Eq. 32)}$$

$$\frac{\partial \langle V \rangle}{\partial t} + \frac{\partial \langle UV \rangle}{\partial x} + \frac{\partial \langle V^2 \rangle}{\partial y} - (WV)_o = f\langle U_g - U \rangle + \overline{vw}_o \qquad \text{(Eq. 33)}$$

$$\frac{D\langle \overline{uu} \rangle}{Dt} = \left\langle 4\Omega\left(\overline{uv} \sin\phi - \overline{uw} \cos\phi\right) - 2\overline{uw} \frac{\partial U}{\partial z} \right\rangle + v_c \left[\Lambda q \frac{\partial \overline{uu}}{\partial z}\right]_o^\infty - \left\langle \frac{q}{\Lambda}\left(\overline{uu} - \frac{q^2}{3}\right) + \frac{2bq^3}{3\Lambda} \right\rangle \qquad \text{(Eq. 34)}$$

$$\frac{D\langle \overline{vv} \rangle}{Dt} = \left\langle -4\Omega\overline{uv} \sin\phi - 2\overline{vw} \frac{\partial V}{\partial z} \right\rangle + v_c \left[\Lambda q \frac{\partial \overline{vv}}{\partial z}\right]_o^\infty - \left\langle \frac{q}{\Lambda}\left(\overline{vv} - \frac{q^2}{3}\right) + \frac{2bq^3}{3\Lambda} \right\rangle \qquad \text{(Eq. 35)}$$

$$\frac{D\langle \overline{ww} \rangle}{Dt} = \left\langle 4\Omega\overline{uw} \cos\phi \right\rangle + v_c \left[\Lambda q \frac{\partial \overline{ww}}{\partial z}\right]_o^\infty - \left\langle \frac{q}{\Lambda}\left(\overline{ww} - \frac{q^2}{3}\right) + \frac{2bq^3}{3\Lambda} \right\rangle \qquad \text{(Eq. 36)}$$

$$\frac{D\langle \overline{uv} \rangle}{Dt} = \left\langle 2\Omega\left(\overline{vv} \sin\phi - \overline{vw} \cos\phi - \overline{uu} \sin\phi\right) - \overline{uw} \frac{\partial V}{\partial z} - \overline{vw} \frac{\partial U}{\partial z} \right\rangle + v_c \left[\Lambda q \frac{\partial \overline{uv}}{\partial z}\right]_o^\infty - \left\langle \frac{q}{\Lambda} \overline{uv} \right\rangle \qquad \text{(Eq. 37)}$$

$$\frac{D\langle \overline{uw} \rangle}{Dt} = \left\langle 2\Omega\left(\overline{vw} \sin\phi - \overline{ww} \cos\phi + \overline{uu} \cos\phi\right) - \overline{ww} \frac{\partial U}{\partial z} \right\rangle + v_c \left[\Lambda q \frac{\partial \overline{uw}}{\partial z}\right]_o^\infty - \left\langle \frac{q}{\Lambda} \overline{uw} \right\rangle \qquad \text{(Eq. 38)}$$

$$\frac{D\langle \overline{vw} \rangle}{Dt} = \left\langle 2\Omega\left(-\overline{uw} \sin\phi + \overline{uv} \cos\phi\right) - \overline{ww} \frac{\partial V}{\partial z} \right\rangle + v_c \left[\Lambda q \frac{\partial \overline{vw}}{\partial z}\right]_o^\infty - \left\langle \frac{q}{\Lambda} \overline{vw} \right\rangle \qquad \text{(Eq. 39)}$$

where

$$\frac{D\langle()\rangle}{Dt} = \frac{\partial\langle()\rangle}{\partial t} + \frac{\partial\langle U()\rangle}{\partial x} + \frac{\partial\langle V()\rangle}{\partial y} - [W()]_o$$

To make this a closed system, we must relate such integrals as $\langle UV\rangle$ to $\langle U\rangle\langle V\rangle$, $\langle\overline{ww}\frac{\partial U}{\partial z}\rangle$ to $\langle\overline{ww}\rangle\langle U\rangle$, etc. This may be done by parameterizing the profile shape of the variable with respect to z. These profile shapes may contain only one independent parameter for each independent variable. Of course, the profile distributions may be chosen to be consistent with as many boundary condition constraints as desired.

To be specific, we will work through a limiting case for a sample choice of profile distributions. To achieve the desired asymptotic approach to geostrophic conditions, we use an exponential z dependence. At the surface we force the profiles to be compatible with the surface layer conditions obtained by requiring that Equations 32-39 also be satisfied across the thin constant flux layer next to the surface. For neutral flow these surface conditions reduce to the familiar law-of-the-wall conditions

$$(U_r^2 + V_r^2)^{1/2} = \frac{u^*}{k}\ln(z_r/z_o) \qquad \text{(Eq. 40)}$$

$$\frac{V_r}{U_r} = \frac{\overline{vw}_r}{\overline{uw}_r} \qquad \text{(Eq. 41)}$$

with

$$u^{*2} = [\overline{uw}_r^2 + \overline{vw}_r^2]^{1/2} \qquad \text{(Eq. 42)}$$

and the turbulent correlations related by their super-equilibrium values (7)

$$q_r^2 = \sqrt{32}u^{*2} \qquad \text{(Eq. 43)}$$

$$\overline{ww}_r = q_r^2/4 \qquad \text{(Eq. 44)}$$

To these constraints we add matching conditions at z_r , the upper edge of the surface layer

$$\left.\frac{\partial U}{\partial z}\right|_r = \frac{u^*}{kz_r}\frac{U_r}{(U_r^2 + V_r^2)^{1/2}} \qquad \text{(Eq. 45)}$$

$$\left.\frac{\partial q^2}{\partial z}\right|_r = 0 \qquad \text{(Eq. 46)}$$

$$\left.\frac{\partial \overline{uw}}{\partial z}\right|_r = fV_r \qquad \text{(Eq. 47)}$$

$$\left.\frac{\partial \overline{vw}}{\partial z}\right|_r = f(U_g - U_r) \qquad \text{(Eq. 48)}$$

For purposes of this sample calculation, we simplify the correlation equations, Equations 34-39, by assuming $\overline{ww} = q^2/4$ and carrying only two integrated equations, one for q^2 and Equation 38 for $\overline{uw}$. With the exception of the Coriolis terms, Equation 39 for $\overline{vw}$ is similar to Equation 38 for $\overline{uw}$. In the present approximation we neglect the Coriolis terms in the shear stress equations so it is consistent to carry only one integral equation for the shear stress. The equation for q^2 is obtained by adding Equations 34 through 36

$$\frac{D\langle q^2\rangle}{Dt} = -\left\langle 2\overline{uw}\frac{\partial U}{\partial z} + \overline{vw}\frac{\partial V}{\partial z} - \frac{2bq^3}{A}\right\rangle \qquad \text{(Eq. 49)}$$

Profile shapes with a total of 10 independent parameters may now be used to approximate the five variables (U , V , $\overline{uw}$, $\overline{vw}$, q). We approximate the profiles as:

$$U_g - U = (U_g - U_r)e^{-\lambda z} \qquad \text{(Eq. 50)}$$

$$V = V_r(1 + a_1 z)e^{-\lambda z} \qquad \text{(Eq. 51)}$$

$$\overline{uw} = \overline{uw}_r(1 + a_2 z)e^{-\lambda z} \qquad \text{(Eq. 52)}$$

$$\overline{vw} = \overline{vw}_r(1 + a_3 z)e^{-\lambda z} \qquad \text{(Eq. 53)}$$

$$q = q_r(1 + a_4 z)e^{-\lambda z} \qquad \text{(Eq. 54)}$$

where z is measured from z_r.

Equations 50-54 yield a closed system when the model scale A is determined. In a general scheme we would want to utilize an integral of the scale equation, but for this simple test we choose to use an expression related to the distance from the ground and the spread of q ; thus we choose

$$A = \alpha(ze^{-\beta z} + z_r) \qquad \text{(Eq. 55)}$$

The parameter β is chosen so that the relationship between A_{max} and the height at which q falls to one-half its maximum value remains constant at 0.21, approximately the same value which would be maintained for the dynamic scale equation in the case of a neutral, steady state boundary layer (25).

Equations 32, 33, 38, and 40-55 form a complete set that may be used to compute the approximate variables as a function of x, y , and t . In the limit of steady, spatially homogeneous flow, the system reduces to a set of algebraic equations to determine the profile shapes as a function of Rossby number, $Ro = U_g/fz_o$. Although the profile shapes are only rough approximations to their true shapes, the integrated variables should be reasonably represented as functions of Ro . A good way to view the results is as plots of u^*/U_g and $\tan^{-1}(V/U)$ versus Ro . The approximate integral results compare with the complete numerical integration of our equations as shown in Figures 18 and 19. The u^* variation is quite reasonable but the surface angle is a little rougher than we would like. This can be adjusted by observing from the exact solutions that the height where q falls

to 10 percent of its maximum value is significantly higher than the height where (U_g-U) falls to 10 percent of its maximum value. If the adjustment is made in the assumed profile shape for z so that it is proportional to $e^{-0.2\lambda z}$ (in Equation 55), then as seen in Figure 19, $\tan^{-1}(V/U)$ agrees much better with the exact solution.

We could, of course, continue this process of modifying the profile choices to increase the accuracy of the approximation, but predicting the integrated variables to within about 10 percent of their exact values (as done by these approximate profile choices) would be adequate for engineering calculations. Note from Equations 32 and 33 that predicting u^* and surface wind shear angle correspond to predicting the boundary layer averaged wind velocities directly for this limiting case.

These sample calculations suggest that a method based on generalizing the above approach to include stability variations and pollution dispersal should be a viable procedure for incorporating second-order closure modeling in practical air quality models.

The model by Busch, Chang, and Anthes (26) is representative of currently available boundary layer models for use with regional air quality models. They suggest a grid with 20 vertical points. Thus, in spite of the fact that our second-order closure model deals with two to three times as many basic equations, our boundary layer averaged model should run computationally several times faster than theirs. Thus, it is quite conceivable that our more sophisticated approach may yield an advantage in both accuracy and computer time. We believe the potential payoff, at least, justifies pursuing the approach further.

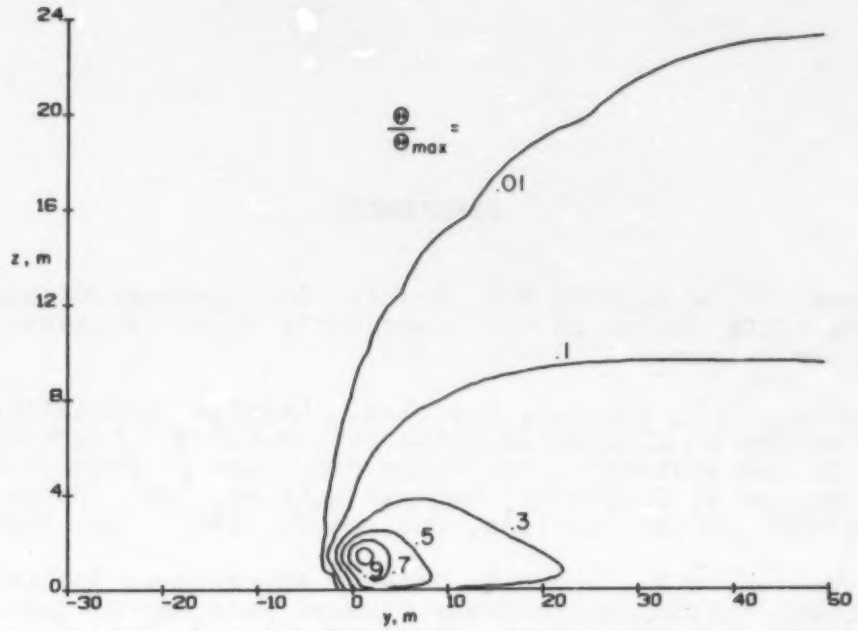

Figure 18. Predicted temperature levels for continous automobile traffic in a surface wind normal to the roadway. Normalization is by local maximum value.

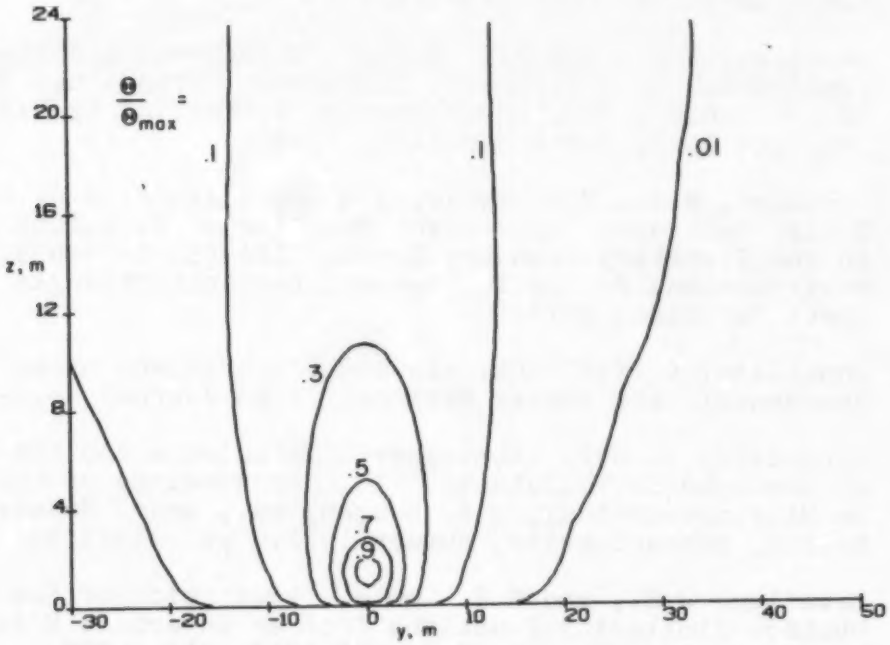

Figure 19. Predicted temperature levels for continous automobile traffic in a surface wind parallel to the roadway. Normalization is by local maximum value.

REFERENCES

1. Lewellen, W.S., and M.E. Teske. Second-Order Closure Modeling of Diffusion in the Atmospheric Boundary Layer. Boundary-Layer Meteor., 10:69-90, 1976.

2. Teske, M.E., and W.S. Lewellen. Example Calculations of At-Atmospheric Dispersion Using Second-Order Closure Modeling. In: Proceedings of the Third Symposium on Atmospheric Turbulence, Diffusion, and Air Quality, Amer. Meteor. Soc., Raleigh, North Carolina, Oct. 19-22, 1976. pp. 149-154.

3. Lewellen, W.S., and M.E. Teske. Atmospheric Pollutant Dispersion Using Second-Order Closure Modeling of the Turbulence. In: Proceedings of the EPA Conference on Environmental Modeling and Simulation, Research Triangle Park, North Carolina, April 19-22, 1976. EPA-600/9-76-106, U.S. Environmental Protection Agency, Research Triangle Park, North Carolina. pp. 714-718.

4. Lewellen, W.S., and M.E. Teske. Turbulence Modeling and Its Application to Atmospheric Diffusion, Parts I and II. EPA-600/4-75-0166, U.S. Environmental Protection Agency, Research Triangle Park, North Carolina, 1975.

5. Lewellen, W.S., M.E. Teske, R.M. Contiliano, G.R. Hilst, and C.duP. Donaldson. Invariant Modeling of Turbulent Diffusion in the Planetary Boundary Layer. EPA-650/4-74-035, U.S. Environmental Protection Agency, Research Triangle Park, North Carolina, 1974.

6. Donaldson, C. duP. Calculation of Turbulent Shear Flows for Atmospheric and Vortex Motions. AIAA Journal, 6:4-12, 1972.

7. Donaldson, C. duP. Atmospheric Turbulence and the Dispersal of Atmospheric Pollutants. In: Proceedings of the Workshop on Micrometeorology, D.A. Haugen, ed., Amer. Meteor. Soc., Boston, Massachusetts, August 1972. pp. 313-390.

8. Lewellen, W.S., and M.E. Teske. Prediction of the Monin-Obukhov Similarity Functions from an Invariant Model of Turbulence. J. Atmos. Sci., 30:1340-1345, 1973.

9. Lewellen, W.S, M.E. Teske, and C.duP. Donaldson. Turbulence Model of Diurnal Variations in the Planetary Boundary Layer. In: Proceedings of the 24th Heat Transfer and Fluid Mechanics Institute, L.R. Davis and R.E. Wilson, eds., Corvallis, Oregon, June 1974. Stanford University Press, Stanford, California, 1974. pp. 301-319.

10. Lewellen, W.S., M.E. Teske, and C.duP. Donaldson. Variable Density Flows Computed by a Second-Order Closure Description of Turbulence. AIAA Journal, 14:382-387, 1976.

11. Launder, B.E., and D.B. Spalding. Mathematical Models of Turbulence. Academic Press, New York, New York, 1972.

12. Lumley, J.L., and B. Khajeh-Nouri. Computational Modeling of Turbulent Transport. Advances in Geophysics, Volume 18A: Academic Press, New York, New York, 1974.

13. Mellor, G.L., and T. Yamada. A Hierarchy of Turbulence Closure Models for Planetary Boundary Layers. J. Atmos. Sci., 31:1791-1806, 1974.

14. Wyngaard, J.C., and O.R. Cote. The Evolution of a Convective Planetary Boundary-Layer - A Higher-Order Closure Model Study. Boundary-Layer Meteor., 7:289-308, 1974.

15. Zeman, O., and J.L. Lumley. Modeling Buoyancy Driven Mixed Layers. J. Atmos. Sci, 33:1974-1988, 1976.

16. Lewellen, W.S., and M.E. Teske. A Second-Order Closure Model of Turbulent Transport in the Coastal Planetary Boundary Layer. In: Proceedings of the Conference on Coastal Meteorology, Amer. Meteor. Soc., Virginia Beach, Virginia, Sept. 1976. pp. 118-123.

17. Buneman, O. A Compact Non-Iterative Poisson Solver. SUIPR Rept. No. 294. Inst. for Plasma Research, Stanford University, Stanford, California, 1969.

18. Swarztrauber, P., and R. Sweet. Efficient Fortran Subprograms for the Solution of Elliptic Partial Differential Equations. Rept. No. NCAR-TN/IA-109. NTIS, Springfield, Virginia, 1975.

19 Kotsovinos, N.E. A Study of the Entrainment and Turbulence in a Plane Buoyant Jet. Rept. No. KH-R-32. Calif. Inst. of Tech., Pasadena, California, 1975.

20. Davies, A.E., J.F. Keffer, and W.D. Baines. Spread of a Heated Plane Turbulent Jet. Physics of Fluids, 18:770-775, 1975.

21. Uberoi, N.S., and P.I. Singh. Turbulent Mixing in a Two-Dimensional Jet. Physics of Fluids, 18:764-769, 1975.

22. Kotsovinos, N.E., and E.J. List. Plane Turbulent Buoyant Jets. Part 1. Integral Properties. J. of Fluid Mech., 81: 25-44, 1977.

23. Briggs, G.A. Plume Rise Predictions. In: Lectures in Air Pollution and Environmental Impact Analysis, D.A. Haugen, ed., Amer. Meteor. Soc., Boston, Massachussetts, Sept. 1975. pp. 59-111.

24. Cederwall, K. Buoyant Slot Jets into Stagnant or Flowing Environments. Rept. No. KH-R-25. Calif. Inst. of Tech., Pasadena, California, 1971.

25. Lewellen, W.S., and G.G. Williamson. Wind Shear and Turbulence Around Airports. Rept. No. NASA-CR-2752. NTIS, Springfield, Virginia, 1976.

26. Busch, N.E., S.W. Chang, and R.A. Anthes. A Multilevel Model of the Planetary Boundary Layer Suitable for Use with Mesoscale Dynamic Models. J. of Appl. Meteor., 15:909-919, 1976.